On the equivalence of binary phase masks optimized for localization or detection in extended depth-of-field localization microscopy

Olivier Lévêque, Caroline Kulcsár, Laurent Cognet, François Goudail

On the equivalence of binary phase masks optimized for localization or detection in extended depth-of-field localization microscopy

OLIVIER LÉVÊQUE,[1,*] CAROLINE KULCSÁR,[1] LAURENT COGNET,[2,3] AND FRANÇOIS GOUDAIL[1]

[1] *Université Paris-Saclay, Institut d'Optique Graduate School, CNRS, Laboratoire Charles Fabry, 91127, Palaiseau, France.*
[2] *Université de Bordeaux, Laboratoire Photonique Numérique et Nanosciences, UMR 5298, 33400, Talence, France.*
[3] *Institut d'Optique & CNRS, LP2N UMR 5298, 33400, Talence, France.*
[*] *olivier.leveque@onera.fr*

Abstract: Binary annular masks have recently been proposed to extend the depth of field (DoF) of single-molecule localization microscopy (SMLM). A strategy for designing optimal masks has been introduced based on maximizing the emitter localization accuracy, expressed in terms of Fisher information, over a targeted DoF range. However the complete post-processing pipeline to localize a single emitter consists of two successive steps: the *detection*, where the regions containing emitters are determined, and the *localization*, where the sub-pixel position of each detected emitter is estimated. Phase masks usually optimize only this second step. The presence of a phase mask also affecting the detection, the purpose of this article is to quantify and mitigate this effect. Using a rigorous framework built from a detection-oriented information theoretical criterion (Bhattacharyya distance), we demonstrate that in most cases of practical significance, annular binary phase masks maximizing Fisher information do also maximize the detection probability. This result supports the common design practice consisting of optimizing a phase mask by maximizing the Fisher information only.

 https://doi.org/10.1364/JOSAA.492654

1. Introduction

Over the past few decades, single-molecule localization microscopy (SMLM) and single particle tracking (SPT) have become indispensable tools for studying the structure and dynamics of biological samples with nanometer resolution [1]. Both approaches conceptually share the same principle: they rely on imaging sequentially single molecules that are sufficiently far away from each other to be optically resolved at the diffraction limit, allowing their individual localization to be determined at nanometer resolution in each image. In SMLM, one observes distinct photo-activatable or blinking molecules in each image of the sequence, whereas in SPT, the same diffusing molecule is tracked through the image sequence. In both modalities, the set of all localizations collected in the image sequence provides structural or dynamic information about the sample under study.

Standard methods localize the molecule in 2D within the imaging plane. However, it is also possible to measure its 3D localization. This can be achieved using spatio-temporally modulated illumination and camera [2] or single pixel imaging [3]. It is also possible to insert a phase mask in the Fourier plane of the microscope [4], or a diffraction grating just before the imaging plane [5], in order to modify the detected point spread function (PSF) in a non-symmetric manner along the optical axis with respect to the imaging plane. Such PSF engineering methods have

been shown to be very efficient to estimate the 3D position of fluorescent emitters within the natural depth of field (DoF) range of the microscope [5, 6]. However, in SMLM and SPT, high numerical aperture (NA) is commonly used to maximize the collection efficiency of the photons emitted by weak single molecule emitters, and to ensure high lateral localization precision. The counterpart is that high NA objectives strongly limit the depth of field (DoF) of the acquired images. Several developments have thus aimed at extending the DoF range of SMLM and SPT microscopes. Two examples of commonly used masks that achieve extended DoF (EDoF) in 3D are the double-helix [7] and the tetrapod [8] masks. The penalty for using such masks is a consequent broadening of the resulting PSFs which thus requires the use of bright emitters or particles for proper super-localization.

In consequence, extending the DoF without trying to localize emitters along the optical axis (*i.e.*, to localize them in 2D along an extended DoF range) can be useful in some applications, since doing so, projection of thick 3D volumes on a 2D plane can be obtained at nanometer resolution [9]. This can be particularly useful in SPT applications that aim to analyze single particle trajectories, such as, for instance, deep-tissue high speed SPT where the number of photons might be too low to apply 3D localization techniques.

For those applications where the depth of the emitter is not estimated using a PSF engineering method, we have recently proposed an optimized annular binary phase mask that extends the microscope DoF range [10] (see Fig. 1). The optimization criterion is based on the Cramér-Rao bound (CRB), which defines the theoretical limit for localization accuracy of a fluorescent emitter in the imaging plane. We have shown that using a mask that minimizes the largest value of the CRB over the targeted EDoF range, and applying an adapted post-processing algorithm, makes it possible to generate excellent 2D super-localization accuracy throughout the desired imaged volume, at the cost of a moderate loss of localization accuracy in the focal plane as compared to the situation where no mask would be used [10]. The effectiveness of these masks was recently demonstrated in a SPT experiment [11].

However, it has to be kept in mind that the complete post-processing pipeline to localize a single emitter in an image consists of two successive steps: the *pre-localization* (also called *detection*), where the regions of the image containing emitters are determined, and the *localization*, where the sub-pixel position of each detected emitter is estimated [12]. Phase masks are usually optimized by taking into account only this second step. However, it is clear that the presence of a phase mask also affects the detection step as well. It is therefore important to quantify the effect that the insertion of a phase mask optimized for localization in the microscope produces on the detection step. This is the question addressed in this article, which is organized as follows. Section 2 defines the imaging model, the microscope DoF range, and the phase mask architecture we use. The pre-localization step of a fluorescent emitter is then formalized in Section 3 as a classification problem. To quantify the effect of a phase mask on detection performance, we propose in Section 4 a detectability metric based on the Bhattacharyya distance [13]. This metric is then used in Section 5 to optimize phase masks for detection over a prescribed DoF range. In Section 6, these optimal masks are compared to the masks that were optimized for localization-only in a previous study [14]. Section 7 is devoted to concluding remarks and perspectives.

2. The depth of field (DoF) and its extension

We consider fluorescent emitters having nanometric size. They can be considered as point-like light sources since their dimensions are not resolved by the microscope. Let us denote the lateral position of an emitter in the sample by the coordinates $\boldsymbol{\theta} = (x_\mathrm{p}, y_\mathrm{p})$ and its longitudinal position (along the optical axis) by the z_p coordinate. It is assumed that the microscope objective is object-space telecentric, aplanatic (*i.e.*, it fulfills the Abbe sine condition), and limited by diffraction over its field of view. As a consequence, the lateral magnification, denoted by M, does not depend on the z_p longitudinal coordinate and the image of the emitter is spatially invariant.

The fluorescence signal distribution in the image plane (on the sensor), at coordinates (x, y), is therefore proportional to:

$$f_{\psi}(x, y, \boldsymbol{\theta}) \propto \left| \int_0^1 J_0 \left(\frac{2\pi \, \mathrm{NA} \, r}{\lambda |M|} \sqrt{\left(x - |M| x_\mathrm{p}\right)^2 + \left(y - |M| y_\mathrm{p}\right)^2} \right) e^{i \Phi_\psi(r)} r \, \mathrm{d}r \right|^2 \tag{1}$$

with $\iint f_{\psi}(x, y, \boldsymbol{\theta}) \, \mathrm{d}x \, \mathrm{d}y = 1$ and where $J_0(\cdot)$ is the Bessel function of the first kind of order 0, λ is the wavelength of the collected light and NA is the object numerical aperture.

The pupil phase function $\Phi_\psi(r)$, involved in Eq. (1), characterizes the phase difference in the exit pupil between a real aberrant wavefront and a spherical reference surface. In the presence of defocus aberration, the function $\Phi_\psi(r)$ is classically described by a quadratic function of the reduced radial pupil coordinate r [15]:

$$\Phi_\psi(r) \simeq \frac{2\pi}{\lambda} \psi r^2 \tag{2}$$

where ψ is the defocus parameter which characterizes the phase deviation $2\pi\psi/\lambda$ at the pupil edge (*i.e.*, when $r = 1$) in the presence of defocus aberration. The parameter ψ has the following expression [16]:

$$\psi \simeq \frac{\mathrm{NA}^2}{2n} \left(z_\mathrm{p} - z_\mathrm{focus} \right) \tag{3}$$

where n is the matched refractive index of the sample and z_focus the position at which the instrument is focused.

When the optical system is perfectly focused on the fluorescent emitter to be imaged (*i.e.*, $z_\mathrm{focus} = z_\mathrm{p}$), there is no defocus aberration. The value of the defocus parameter ψ is then equal to 0, which cancels the pupil phase function $\Phi_\psi(r)$ defined in Eq. (2). The PSF defined in Eq. (1) is then described by the Airy spot:

$$f_\mathrm{Airy}(x, y, \boldsymbol{\theta}) \propto \left| \frac{J_1 \left(\frac{2\pi \, \mathrm{NA}}{\lambda |M|} \sqrt{\left(x - |M| x_\mathrm{p}\right)^2 + \left(y - |M| y_\mathrm{p}\right)^2} \right)}{\frac{2\pi \, \mathrm{NA}}{\lambda |M|} \sqrt{\left(x - |M| x_\mathrm{p}\right)^2 + \left(y - |M| y_\mathrm{p}\right)^2}} \right|^2 \tag{4}$$

where J_1 denotes the Bessel function of the first kind of order 1.

In the presence of defocus aberration (*i.e.*, $|\psi| > 0$), the PSF of the imaging system degrades. If the Rayleigh criterion is respected (*i.e.*, $|\psi| \leq \lambda/4$), the central value of the PSF decreases by more than 20% with an almost negligible deformation of the Airy spot. It is therefore common to define the natural DoF of the microscope by the interval $\psi \in [-\lambda/4, \lambda/4]$.

To extend the DoF of an imaging system without changing its aperture, a phase mask can be placed in its exit pupil [17]. The mask introduces a phase modulation in the aperture stop that modifies the PSF so that it becomes less sensitive to defocus aberration. Several mask architectures can be used. In this paper, we consider annular binary phase masks which have the advantage of being easy to manufacture while having a DoF extension capacity equivalent to that of masks whose phase varies continuously [18]. These masks are composed of concentric rings, as shown in Fig. 1. A mask with L rings and unit aperture radius is defined by the set of its $L - 1$ radii represented by the vector $\boldsymbol{\rho} = (\rho_1, \cdots, \rho_{L-1})$. Each ring adds to the incident wavefront a phase of 0 or π radians at the nominal wavelength λ of the incident light. Thus, in the presence of defocus aberration and a phase mask, the pupil phase function defined in Eq. (2) becomes:

$$\Phi_\psi(r) \simeq \frac{2\pi}{\lambda} \psi r^2 + \Phi_\mathrm{mask}(r, \boldsymbol{\rho}) \tag{5}$$

where $\Phi_\mathrm{mask}(r, \boldsymbol{\rho})$ denotes the binary phase function of the mask (0 or π radians) and $\boldsymbol{\rho}$ its parameter vector.

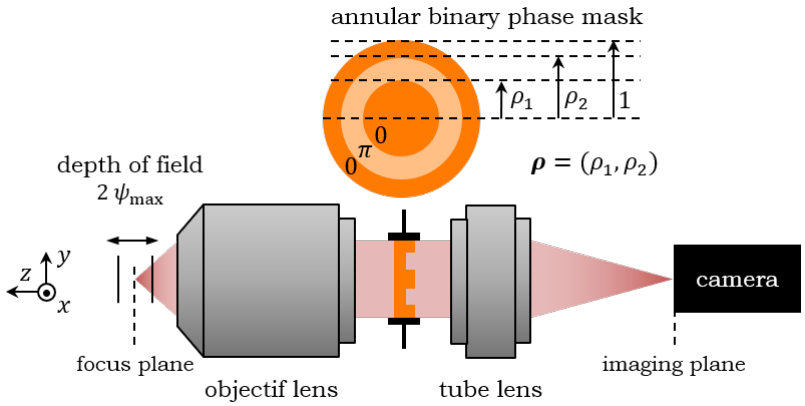

Fig. 1. Schematic diagram of an optical microscope whose its DoF has been extended by placing an optimized annular binary phase mask in the aperture stop of its objective.

3. Statistical hypothesis testing

The detection of a fluorescent emitter can be formulated as a classification problem, where the acquired data are automatically distinguished according to whether or not they contain a fluorescence signal from an emitter. For that purpose, let us consider a thumbnail of size $(2P+1) \times (2P+1)$ pixels and define the two following hypotheses.

Hypothesis H1: One emitter (and only one) is present in the thumbnail. The signal measured at pixel (i, j) is denoted by s_{ij} and consists of the fluorescence signal from the emitter and of a spatially constant background of mean b coming from *e.g.* from the electronic offset of the sensor or from the autofluorescence of the biological medium. Since both signals are disturbed by shot noise, the discrete random variable s_{ij} under the hypothesis H1 is a Poisson distribution:

$$P_{1,ij}[k] = \frac{\lambda_{1,ij}^k}{k!} \exp\left(-\lambda_{1,ij}\right) \tag{6}$$

with mean equal to

$$\lambda_{1,ij} = N_0 \mu_{ij}^{\psi,\boldsymbol{\theta}} + b \ . \tag{7}$$

In this equation, N_0 denotes the average number of photo-electrons measured from the emitter and $\mu_{ij}^{\psi,\boldsymbol{\theta}}$ corresponds to the value of the imaging system PSF, defined in Eq. (1), integrated over the square pixel (i, j) of side length Δ_{xy}:

$$\mu_{ij}^{\psi,\boldsymbol{\theta}} = \int_{(i-\frac{1}{2})\Delta_{xy}}^{(i+\frac{1}{2})\Delta_{xy}} \int_{(j-\frac{1}{2})\Delta_{xy}}^{(j+\frac{1}{2})\Delta_{xy}} f_\psi(x, y, \boldsymbol{\theta})\, \mathrm{d}x\, \mathrm{d}y \ . \tag{8}$$

Hypothesis H0: There is no fluorophore in the thumbnail; only the background signal is measured. The probability distribution of the discrete random variable s_{ij} under this hypothesis is denoted by $P_0[k]$. It is again a Poisson distribution, as defined in Eq. (6), but with a mean independent of the pixel (i, j):

$$\lambda_0 = b \ . \tag{9}$$

Figure 2 illustrates these two hypotheses by a set of simulated thumbnails in which an emitter is either absent [see Fig. 2(a)] or present [see Figs. 2(b-d)] with three different values of the

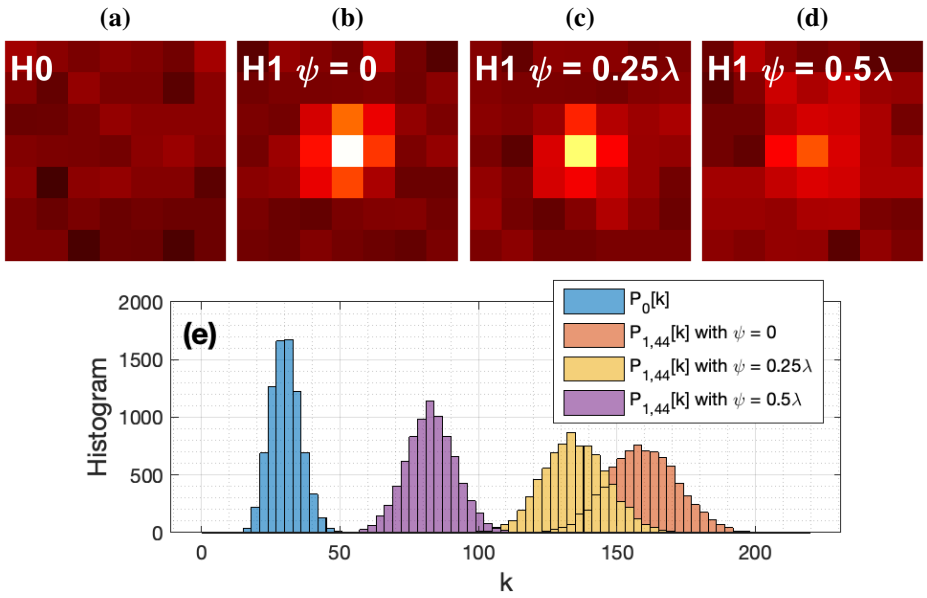

Fig. 2. **(a-d)** Simulations of thumbnails $\underline{s}$ verifying the H0 or H1 hypothesis for optical microscopes without phase mask and for several values of the defocus parameter ψ. **(e)** Histogram of the value of the central pixel $(i, j) = (4, 4)$ made on 8 000 noise realizations. The microscope configuration and the simulation parameters are defined in Table 1 with $N_0 = 500$ ph.e$^-$ and $b = 30$ ph.e$^-$.

defocus parameter ψ, namely $\psi = \{0, 0.25\lambda, 0.5\lambda\}$. Figure 2(e) represents the histogram of the central pixel value constructed from 8 000 different noise realizations. These numerical simulations are carried out with the parameters described in Table 1. It is clearly seen that as the defocus parameter ψ increases, the PSF degrades: it spreads and disappears in the background fluorescence. With the naked eye, comparing Fig. 2(d) with Fig. 2(a), it is clear that it will become increasingly difficult to determine whether a fluorophore is present or not. This is also seen in Fig. 2(e), where the histogram associated with the central pixel $P_{1,44}[k]$ approaches $P_0[k]$ as ψ increases: the hypotheses H1 and H0 will "merge" and become less and less discernible.

A decision algorithm consists in automatically classifying the acquired data sets $\underline{s} = (s_{ij})_{(i,j)\in[-P,P]^2}$ by distinguishing those containing a fluorescence signal (*i.e.*, verifying the hypothesis H1) and those that are empty (*i.e.*, verifying the hypothesis H0). Neyman *et al.* showed in 1933 that the optimal algorithm — *i.e.*, the one that gives the maximal detection probability for a given probability of false alarm — consists in comparing the likelihood ratio to a threshold [19].

4. Bhattacharyya distance

No hypothesis test, even the optimal one like Neyman *et al.*'s, can lead to a perfect classification. Moreover, as shown in Fig. 2, it is expected that the farther a fluorophore is from the focal plane (*i.e.*, $|\psi|$ large), the less discernible the H1 and H0 hypotheses, and the more difficult the classification problem. In order to evaluate the performance of a hypothesis testing algorithm, we can compute its error probability, that is, the probability that a thumbnail $\underline{s}$ is assigned to the wrong class.

The Bayes error rate ϵ is the smallest possible error probability that a classification algorithm can lead to [19]. Since under both hypotheses H1 and H0 the measured pixel values s_{ij} are

Simulation parameters	Symbols	Values
Fluorophore position in the plane	$(x_\mathrm{p}, y_\mathrm{p})$	$(0, 0)$ µm
Fluorophore wavelength emission	λ	700 nm
PSF image length	$2P + 1$	21 pixels
Pixel length	Δ_{xy}	10 µm
Object numerical aperture	NA	1.3
Lateral magnification	M	60

Table 1. Microscope configuration and simulation parameters used.

statistically independent of each other, the expression of ϵ depends on $P_{1,ij}[k]$ and $P_0[k]$ as follows [20]:

$$\epsilon = \sum_{s_{11},s_{12},s_{21},\cdots} \min\left\{ p_1 \prod_{i=-P}^{P} \prod_{j=-P}^{P} P_{1,ij}[s_{ij}]; p_0 \prod_{i=-P}^{P} \prod_{j=-P}^{P} P_0[s_{ij}] \right\} \tag{10}$$

with p_1 and p_0 the prior probabilities of the hypotheses H1 and H0. The sum is performed on all possible values of the $(2P + 1)^2$ pixels, so that $s_{ij} = \{0, 1, \cdots, +\infty\}$. Using the inequality $\min\{a; b\} \leq a^\gamma b^{1-\gamma}$ (where a, $b \geq 0$ and $0 \leq \gamma \leq 1$), it is easily seen that Eq. (10) can be upper bounded by:

$$\epsilon_u(\gamma) = \exp\left[- \sum_{i=-P}^{P} \sum_{j=-P}^{P} C_{ij}(\gamma) \right] \qquad 0 \leq \gamma \leq 1 \tag{11}$$

where

$$C_{ij}(\gamma) = -\ln\left[\sum_{k=0}^{+\infty} P_{1,ij}[k]^\gamma P_0[k]^{1-\gamma} \right] \tag{12}$$

is the Chernoff distance between the probability laws $P_{1,ij}[k]$ and $P_0[k]$ [21]. Since these laws follow Poisson distributions of means $\lambda_{1,ij}$ and λ_0 respectively, as defined in Eqs. (7) and (9), the Chernoff distance has the following closed-form expression:

$$C_{ij}(\gamma) = \gamma\lambda_{1,ij} + (1 - \gamma)\lambda_0 - \lambda_{1,ij}^\gamma \lambda_0^{1-\gamma} \ . \tag{13}$$

Thus, the smallest upper bound on ϵ (also called the Chernoff bound) is obtained with the value of γ that maximizes the sum of $C_{ij}(\gamma)$. This optimal value depends on the means $\lambda_{1,ij}$ and λ_0 and has no closed-form expression. However, it can be shown that for many applications, the optimal value of γ is close to 0.5 [22]. This is what can be observed in Fig. 3, where the optimal value of the parameter γ is plotted as a function of the defocus parameter ψ for data simulated with the parameters defined in Table 1: for all the considered values of ψ, the Chernoff bound is reached for a value of γ close to 0.5.

Thus, $\epsilon_u(0.5)$ is a good candidate to characterize the detectability of a fluorophore since it allows to approach the Chernoff bound by a closed-form expression. This metric, which is called the Bhattacharyya distance [13], has the following expression:

$$\mathcal{B}(\boldsymbol{\rho}, \psi) = \sum_{i=-P}^{P} \sum_{j=-P}^{P} C_{ij}(0.5) = \frac{b}{2} \sum_{i=-P}^{P} \sum_{j=-P}^{P} \left(\sqrt{\frac{N_0}{b} \mu_{ij}^{\psi,\boldsymbol{\theta}} + 1} - 1 \right)^2 \tag{14}$$

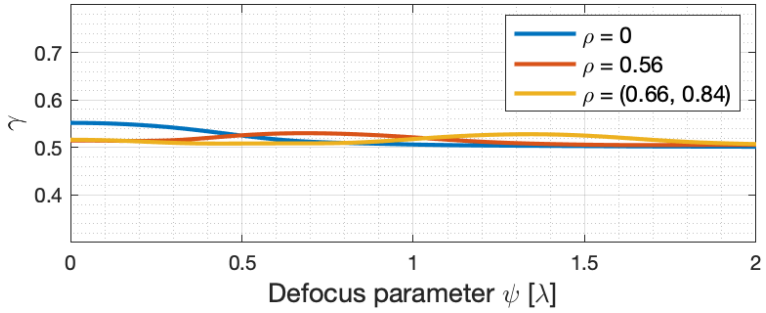

Fig. 3. Optimal value of the parameter γ, which minimizes the upper bound of the Bayes error rate $\epsilon_u(\gamma)$. This value is plotted as a function of the defocus parameter ψ for different mask parameters $\boldsymbol{\rho}$. The microscope configuration and the simulation parameters used are defined in Table 1 with N_0 = 500 ph.e$^-$ and b = 30 ph.e$^-$.

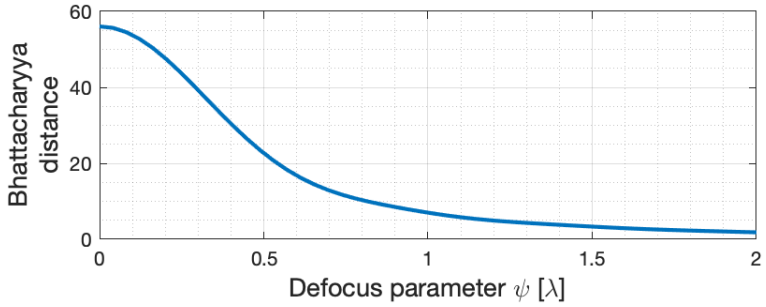

Fig. 4. Evolution of the Bhattacharyya distance for an optical system without phase mask ($\boldsymbol{\rho}$ = 0) as a function of the defocus parameter ψ. The microscope configuration and the simulation parameters used are defined in Table 1 with N_0 = 500 ph.e$^-$ and b = 30 ph.e$^-$.

where we have explicitly indicated its dependence on the mask parameter vector $\boldsymbol{\rho}$ and on the defocus parameter ψ. It allows us to evaluate the intrinsic difficulty of a detection problem in the presence of spatially uncorrelated Poisson noise. The interest of using Eq. (14) as a measure of contrast in imaging science has been illustrated in Refs. [22] and [23].

The Bhattacharyya distance $\mathcal{B}$ can be interpreted as a measure of similarity (or separability) between the hypotheses H0 and H1. It will therefore be used to evaluate the intrinsic ability with which the fluorescence signal of an emitter can be detected in a measured image. As an illustration, Fig. 4 represents the evolution of the distance $\mathcal{B}$ in Eq. (14) for an optical system without phase mask ($\boldsymbol{\rho}$ = 0) as a function of the defocus parameter ψ. We observe that it decreases as ψ increases. In other words, the hypotheses H1 and H0 are less and less discernible. This logical result quantifies the fact that a fluorophore far from the focal plane ($|\psi| > 0$) is more difficult to detect than when it is located in the focal plane (ψ = 0).

5. Phase mask optimization for detection applications

To extend the depth over which fluorescent emitters can be detected, we propose to optimize annular binary phase masks using the criterion based on the Bhattacharyya distance defined in Eq. (14). A reasonable criterion for mask optimization is to maximize the smallest value of the Bhattacharyya distance within the targeted EDoF range $[-\psi_{\max}, \psi_{\max}]$. The optimal mask parameters, denoted by the vector $\boldsymbol{\rho}_{\text{opt}}$, are thus obtained by solving the following optimization

problem:

$$\boldsymbol{\rho}_{\text{opt}} = \arg\max_{\boldsymbol{\rho}} J_{\text{det}}(\boldsymbol{\rho}) \qquad \text{with} \qquad J_{\text{det}}(\boldsymbol{\rho}) = \min_{\psi \in [-\psi_{\max}, \psi_{\max}]} \mathcal{B}(\boldsymbol{\rho}, \psi) \ . \tag{15}$$

Given the expression of $\mathcal{B}$ in Eq. (14), the optimal mask parameters $\boldsymbol{\rho}_{\text{opt}}$ depend on the experimental conditions through the ratio N_0/b, which will be called the *photon balance* in the following. Since the cost function $J_{\text{det}}(\boldsymbol{\rho})$ is highly non-convex, Eq. (15) is solved using the particle swarm optimization algorithm [24]. This approach relies on the collaboration of individuals. Based on simple displacement rules, a set of particles (whose coordinates describe the radii of the rings of a binary annular mask) explore the optimization landscape and gradually converge together towards a local minimum. Since there is no guarantee of finding the global minimum, different runs may converge to different optimal masks with similar performance. The optimization is performed with ring structures composed of a maximum of $L = 5$ rings. However, considering the optical parameters of Table 1 and N_0/b values belonging to the interval $[8, 500]$, we observed that the mask performance stabilizes from a number lower than 5 rings. The optimal mask parameters $\boldsymbol{\rho}_{\text{opt}}$ also depend on the lateral emitter position with respect to the pixel grid. However, one can show by simulation that this position has very little influence on the optimal mask parameters $\boldsymbol{\rho}_{\text{opt}}$. To facilitate the comparison between the masks that are optimal for detection and those optimal for localization obtained in Ref. [14], we will assume that the emitter is located at the center of a pixel so that $\boldsymbol{\theta}_0 = (0, 0)$.

Figure 5(a) plots the optimal mask parameters as a function of the photon balance N_0/b for three different targeted DoF ranges: $\psi_{\max} = \{1\lambda, 1.5\lambda, 2\lambda\}$. For a given value of N_0/b, the mask parameters are represented by a vertical set of points: each point characterizes the radius ρ_ℓ of a ring with $\ell \in \{1, \cdots, L-1\}$ (radii equal to 0 or 1 are not represented). The performance of the masks is displayed using solid markers (associated with the legend "Detection") in Fig. 5(b) for $\psi_{\max} = 1\lambda$, in Fig. 5(c) for $\psi_{\max} = 1.5\lambda$ and in Fig. 5(d) for $\psi_{\max} = 2\lambda$. In these figures, the mask performance is normalized by dividing the optimal value of the criterion $J_{\text{det}}(\boldsymbol{\rho}_{\text{opt}})$ by $J_{\text{det}}(0)$ the value of the criterion obtained without a mask. We will comment in detail the curves with hollow markers in the next paragraph.

Let us first analyze the results obtained for a targeted DoF range of $\psi_{\max} = 1\lambda$. In Fig. 5(a) (solid blue round markers), it is observed that whatever the value of N_0/b, the optimal masks are composed of only $L = 2$ rings. When $N_0/b < 200$, the parameter ρ_1 of the optimal mask increases almost linearly from 0.56 to 0.66. It then stabilizes at $\rho_1 = 0.68$ when $N_0/b \in [200, 450]$, and then when $N_0/b > 450$, ρ_1 is zero: the optimal configuration corresponds to the absence of a mask. Moreover, we observe in Fig. 5(b) (solid blue round markers) that the performance gap between the cases with and without mask is larger for small values of N_0/b. For example, when $N_0/b = 8$, we obtain $J_{\text{det}}(\boldsymbol{\rho}_{\text{opt}}) = 1.78 \times J_{\text{det}}(0)$.

The use of a phase mask therefore significantly improves the detection of fluorophores. Small values of N_0/b correspond to situations where the dominant source of noise is due to background fluctuations (we shall call this situation *Scenario B*, as in Ref. [14]). In this scenario, the PSF of the imaging system is drowned in the background noise when no mask is used. The optimal mask allows the PSF to be modified in order to improve the contrast between the fluorophore image and the background.

We also observe that $J_{\text{det}}(\boldsymbol{\rho}_{\text{opt}})$ tends asymptotically to $J_{\text{det}}(0)$ as the photon balance N_0/b increases, that is, when the dominant source of noise is the shot noise due to the fluorescence signal (this situation is called *Scenario A* in Ref. [14]). It means that in this case, the use of a phase mask does not improve nor deteriorate fluorophore detection: the contrast between the fluorophore and the background is sufficient for a correct detection over the DoF range $\psi_{\max} = 1\lambda$ without the help of a mask.

To explain this fact, we can notice that if the fluorescence signal is such that $N_0 \mu_{ij}^{\psi, \boldsymbol{\theta}_0} \gg b$

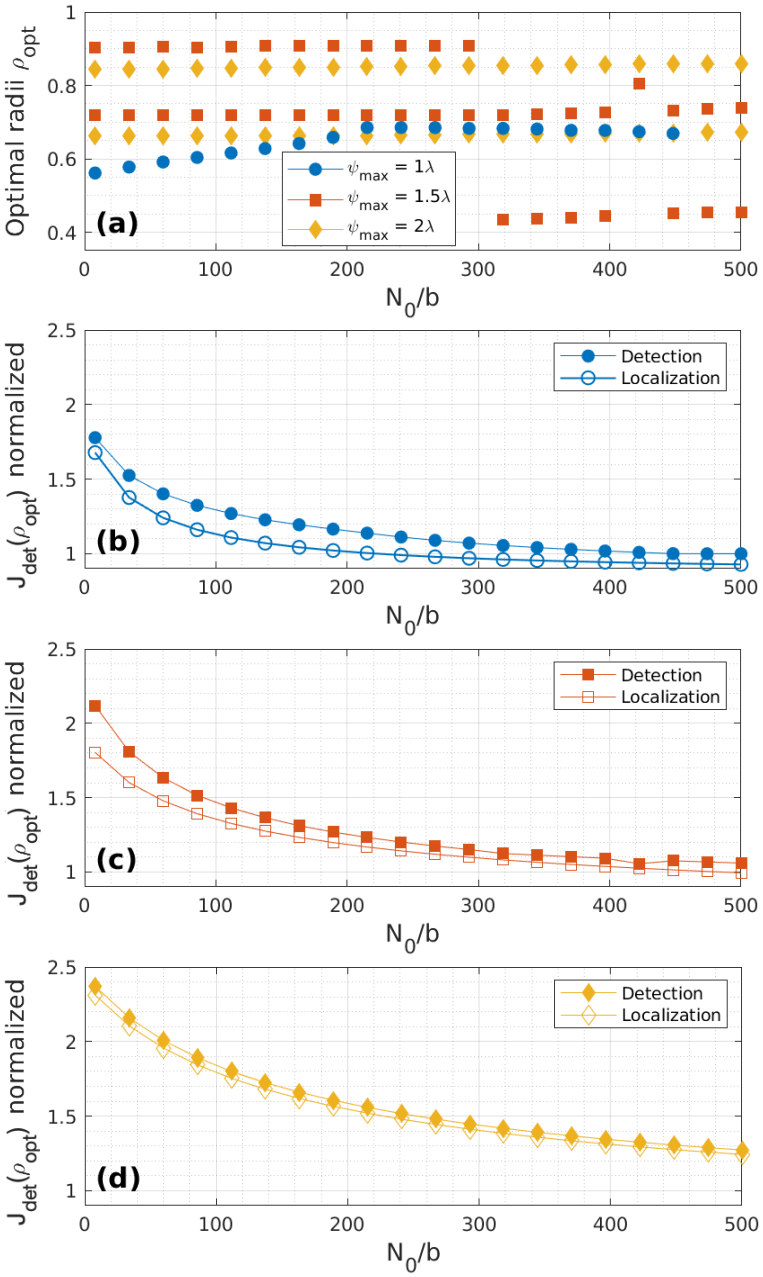

Fig. 5. **(a)** Evolution of the optimal annular binary phase mask parameters $\boldsymbol{\rho}_{\text{opt}}$, defined in Eq. (15), as a function of the photon balance N_0/b with $\psi_{\text{max}} = \{1\lambda, 1.5\lambda, 2\lambda\}$. **(b-d)** Comparison of normalized detection criterion values, *i.e.*, $J_{\text{det}}(\boldsymbol{\rho}_{\text{opt}})/J_{\text{det}}(0)$, respectively computed with optimal masks defined in Eqs. (15) and (20), for (b) $\psi_{\text{max}} = 1\lambda$, (c) 1.5λ and (d) 2λ. The microscope configuration and the simulation parameters used are defined in Table 1 with $N_0/b \in [8, 500]$.

(Scenario A), then the Bhattacharyya distance $\mathcal{B}$ defined in Eq. (14) becomes:

$$\mathcal{B} \simeq \frac{N_0}{2} \sum_{i=-P}^{P} \sum_{j=-P}^{P} \mu_{ij}^{\psi,\boldsymbol{\theta}_0} \ . \tag{16}$$

This approximate expression no longer depends on the parameters $\boldsymbol{\rho}$ and ψ since the conservation of energy by a phase mask imposes:

$$\sum_{i=-P}^{P} \sum_{j=-P}^{P} \mu_{ij}^{\psi,\boldsymbol{\theta}_0} = \text{constant} \ . \tag{17}$$

Thus, the criterion $J_{\text{det}}(\boldsymbol{\rho}_{\text{opt}})$ defined in Eq. (15) tends asymptotically to $J_{\text{det}}(0)$.

As ψ_{max} increases, it is seen in Fig. 5(a) that the optimal masks are composed of a larger number of rings: whereas for $\psi_{\text{max}} = 1\lambda$, the optimal mask consists of $L = 2$ rings, it is composed of $L = 3$ rings for $\psi_{\text{max}} = 1.5\lambda$ or 2λ. This reflects the increasing difficulty of optimizing a phase mask as the targeted DoF range widens. This result is similar to the one established for imaging or localization, where the number of rings of the optimal mask also increases with ψ_{max} [10, 25]. Moreover, the conclusions previously established in Fig. 5(b) for the DoF range $\psi_{\text{max}} = 1\lambda$ remain similar when $\psi_{\text{max}} = 1.5\lambda$ (see solid markers in Fig. 5(c)) or 2λ (see solid markers in Fig. 5(d)): the performance gap between the cases with and without mask is maximum for $N_0/b = 8$ and decreases as the photon balance increases. This means that $J_{\text{det}}(\boldsymbol{\rho}_{\text{opt}})$ tends to $J_{\text{det}}(0)$ when N_0/b increases.

We can also notice in Fig. 5(a) that as the targeted DoF range ψ_{max} widens, the optimal mask parameters vary less and less as a function of the photon balance N_0/b. This result can be explained by a conjecture established in Ref. [14] and observed in Figs. 2(b-d): for the same value of N_0/b, the PSF spreads and drowns into the background noise as ψ_{max} increases. In this case, the inequality $N_0 \mu_{ij}^{\psi,\boldsymbol{\theta}_0} \ll b$ (Scenario B) is even more valid and the Bhattacharyya distance $\mathcal{B}$ is approximated by:

$$\mathcal{B}(\boldsymbol{\rho}, \psi) \simeq \frac{1}{8} \frac{N_0^2}{b} \sum_{i=-P}^{P} \sum_{j=-P}^{P} \left(\mu_{ij}^{\psi,\boldsymbol{\theta}_0} \right)^2 \ , \tag{18}$$

and becomes proportional to the signal-to-noise ratio N_0^2/b. Thus, the optimal parameter vector $\boldsymbol{\rho}_{\text{opt}}$ that minimizes the criterion $J_{\text{det}}(\boldsymbol{\rho})$ no longer depends on N_0/b. As a consequence, the optimal masks shown in Fig. 5(a) vary less and less with the photon balance as ψ_{max} increases.

To conclude, the use of an optimal mask for detection applications is only necessary for experimental conditions corresponding to the Scenario B (background noise dominant). For other experimental conditions, the fluorophore image is sufficiently contrasted and the use of the phase mask is no longer necessary for detection.

6. Comparison of masks optimal for detection and for localization

As mentioned in the Introduction, once the fluorescent emitter is detected, its position is finally estimated with a sub-pixel resolution in the localization step.

In general, phase masks are never optimized for detection [8, 26]. For example, we have optimized binary annular phase masks based solely on localization accuracy in Refs. [10] and [14]. In this case, the optimization criterion is based on the Fisher information matrix [20], which quantifies the difficulty of estimating the lateral fluorophore position $\boldsymbol{\theta} = (x_{\text{p}}, y_{\text{p}})$, independently of the (unbiased) algorithm used to perform this estimation. We have shown in Ref. [14] that since the pixelated PSF described in Eq. (8) has almost circular symmetry, the non-diagonal

terms of the Fisher information matrix are negligible. Moreover, when $\boldsymbol{\theta}_0 = (0, 0)$, the diagonal terms are strictly equal and reach their minima. In this case, the Fisher information matrix is then characterized by a single scalar value equal to:

$$\mathcal{I}(\boldsymbol{\rho}, \psi) = \sum_{i=-P}^{P} \sum_{j=-P}^{P} \frac{N_0^2 M^2}{N_0 \mu_{ij}^{\psi,\boldsymbol{\theta}_0} + b} \left(\frac{\partial \mu_{ij}^{\psi,\boldsymbol{\theta}_0}}{\partial x} \right)^2 . \tag{19}$$

To improve the localization accuracy of fluorescent emitters over a targeted EDoF range, annular binary phase masks were optimized by solving the following problem:

$$\boldsymbol{\rho}_{\text{opt}} = \arg\max_{\boldsymbol{\rho}} J_{\text{loc}}(\boldsymbol{\rho}) \qquad \text{with} \qquad J_{\text{loc}}(\boldsymbol{\rho}) = \min_{\psi \in [-\psi_{\max}, \psi_{\max}]} \mathcal{I}(\boldsymbol{\rho}, \psi) \ . \tag{20}$$

Optimal masks for Scenario A ($N_0 \mu_{ij}^{\psi,\boldsymbol{\theta}_0} \gg b$) and Scenario B ($N_0 \mu_{ij}^{\psi,\boldsymbol{\theta}_0} \ll b$) have been determined in Ref. [14].

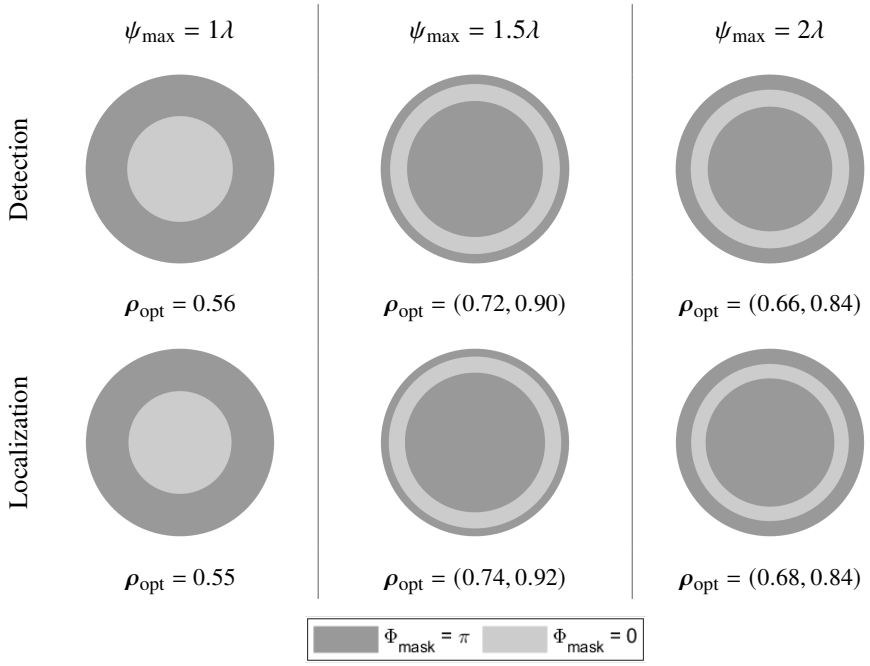

Table 2. Annular binary phase masks obtained by solving Eq. (15) [first row] and Eq. (20) [second row] for a EDoF range such that $\psi_{\max} = \{1\lambda, 1.5\lambda, 2\lambda\}$. The simulation parameters are those defined in Table 1 with $N_0/b = 8$.

We have shown in Section 5 that the use of an optimal mask for detection is only necessary in experimental conditions corresponding to Scenario B, which corresponds to dominant background fluctuations. Thus, we compare in this section the annular binary phase masks optimal for detection and localization in this scenario. These masks are represented in Table 2, where the first row corresponds to the masks optimal for detection when $N_0/b = 8$, that have been represented in Fig. 5, and the second row corresponds to those optimized in Ref. [14] for localization under Scenario B.

We notice that the masks optimized for detection are similar to those optimized for localization. For example, when $\psi_{\max} = 1$ the optimal mask for detection is composed of 2 rings with

$\boldsymbol{\rho}_{\text{opt}} = 0.56$ while the one optimized for localization has also 2 rings and $\boldsymbol{\rho}_{\text{opt}} = 0.55$. Furthermore, when $\psi_{\max} = 1.5\lambda$, it is seen in Fig. 5(a) that the optimal mask for detection has 3 rings and $\boldsymbol{\rho}_{\text{opt}} = (0.72, 0.90)$, while the one optimal for localization has also 3 rings with $\boldsymbol{\rho}_{\text{opt}} = (0.74, 0.92)$. The same result is found when $\psi_{\max} = 2\lambda$: the optimal mask for detection has $\boldsymbol{\rho}_{\text{opt}} = (0.66, 0.84)$ and the one optimal for localization $\boldsymbol{\rho}_{\text{opt}} = (0.68, 0.84)$.

This remarkable similarity can be theoretically explained by analyzing the optimization criteria for detection and localization defined respectively in Eqs. (15) and (20) when the photon balance is small. Indeed, if we assume that $N_0 \mu_{ij}^{\psi,\boldsymbol{\theta}_0} \ll b$, these criteria can be respectively approximated by

$$J_{\text{det}}(\boldsymbol{\rho}) \simeq \min_{\psi \in [-\psi_{\max}, \psi_{\max}]} \sum_{i=-P}^{P} \sum_{j=-P}^{P} \left(\mu_{ij}^{\psi,\boldsymbol{\theta}_0}\right)^2 \tag{21}$$

and

$$J_{\text{loc}}(\boldsymbol{\rho}) \simeq \min_{\psi \in [-\psi_{\max}, \psi_{\max}]} \sum_{i=-P}^{P} \sum_{j=-P}^{P} \left(\frac{\partial \mu_{ij}^{\psi,\boldsymbol{\theta}_0}}{\partial x}\right)^2 , \tag{22}$$

where the pixelated PSF verifies Eq. (17). We notice that maximizing the criteria given in Eqs. (21) and (22) under this constraint corresponds to searching for a phase mask producing PSFs as concentrated as possible on a small number of pixels.

To verify this conjecture, Figs. 6 and 7 display the cost functions $J_{\text{det}}(\boldsymbol{\rho})$ and $J_{\text{loc}}(\boldsymbol{\rho})$ respectively defined in Eqs. (15) and (20) as a function of the mask parameters $\boldsymbol{\rho}$. The experimental conditions used for the simulation are those described in Table 1 with $N_0 = 500$ ph.e$^-$ and $b = 30$ ph.e$^-$ (*i.e.*, $N_0/b = 16.7$). Figure 6 represents the optimization landscapes for detection (solid blue line) and localization (dashed red line) of a 2-ring binary mask defined by its radius ρ_1, for $\psi_{\max} = 1\lambda$ and $N_0/b = 16.7$. We notice that these two optimization landscapes have similar shapes and reach their local extrema for almost the same parameter value ρ_1. For $\psi_{\max} = 1.5\lambda$ and $N_0/b = 16.7$, Fig. 7(a) represents the 3-ring mask optimization landscape for detection as a function of its radii (ρ_1, ρ_2), and Fig. 7(b) is the optimization landscape for localization. We notice again that these two optimization landscapes have similar shapes and almost the same extrema — thus, almost the same optimal masks — that are indicated by a white cross.

The conditions of Scenario B (small number of useful photons and strong background), are the most demanding and frequently encountered in practice. We have shown that in these conditions, the EDoF masks optimized for detection and localization are identical. This result shows that the optimization method based on Fisher information to extend DoF that has been introduced in Ref. [10] optimizes both detection probability and localization accuracy.

In order to quantify the loss of detection performance that would result from using localization-optimized masks, we have plotted in Figs. 5(b)-5(d), with hollow markers, the normalized values of the detection criterion obtained by these masks, respectively for $\psi_{\max} = \{1\lambda, 1.5\lambda, 2\lambda\}$, as a function of the photon balance N_0/b. We note that whatever the value of N_0/b, $J_{\text{det}}(\boldsymbol{\rho}_{\text{opt}}^{\text{loc}})$ (hollow markers) is always lower than $J_{\text{det}}(\boldsymbol{\rho}_{\text{opt}}^{\text{det}})$ (solid markers) where $\boldsymbol{\rho}_{\text{opt}}^{\text{loc}}$ refers to masks optimized for localization with Eq. (20) and $\boldsymbol{\rho}_{\text{opt}}^{\text{det}}$ masks optimized for detection with Eq. (15). The difference between these two curves quantifies the relative loss (expressed as a fraction of $J_{\text{det}}(0)$) caused by the use of a mask optimized for localization. We can see that this relative loss does not exceed 17% when $\psi_{\max} = 1\lambda$, 30% when $\psi_{\max} = 1.5\lambda$ and 6% when $\psi_{\max} = 2\lambda$. We therefore conclude that the masks optimized for localization only slightly degrade the probability of detection compared to the masks that optimize it.

7. Conclusion

We have investigated the DoF extension problem for single-molecule localization microscopy, focusing on the pre-localization step. After defining a rigorous framework built with an explicit

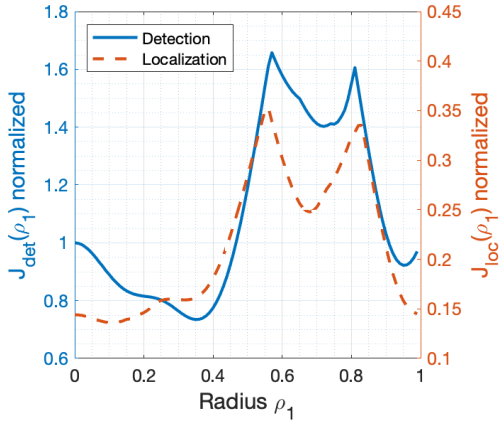

Fig. 6. Optimization landscapes of a 2-ring binary phase mask for detection (solid blue line) and localization (dashed red line) when $\psi_{\max} = 1\lambda$. The values of $J_{\text{det}}(\boldsymbol{\rho})$ defined in Eq. (15) and $J_{\text{loc}}(\boldsymbol{\rho})$ defined in Eq. (20) are normalized by dividing them by $J_{\text{det}}(0)$ and $\mathcal{I}(0,0)$ respectively. The simulation parameters are given in Table 1 with $N_0 = 500$ ph.e$^-$ and $b = 30$ ph.e$^-$.

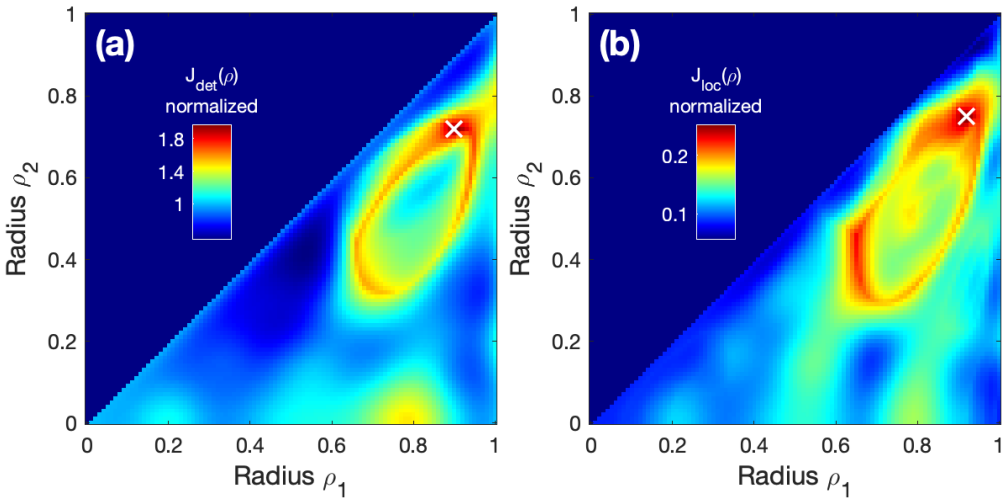

Fig. 7. Optimization landscapes of a 3-ring binary phase mask for **(a)** detection and **(b)** localization applications when $\psi_{\max} = 1.5\lambda$. The values of $J_{\text{det}}(\boldsymbol{\rho})$ defined in Eq. (15) and $J_{\text{loc}}(\boldsymbol{\rho})$ defined in Eq. (20) are normalized by dividing them by $J_{\text{det}}(0)$ and $\mathcal{I}(0,0)$ respectively. The white cross corresponds to the global minimum of the criterion. $[\rho_1, \rho_2]$ are respectively equal to $[0.90, 0.72]$ for detection and $[0.92, 0.75]$ for localization. The simulation parameters are given in Table 1 with $N_0 = 500$ ph.e$^-$ and $b = 30$ ph.e$^-$.

and general information theoretical criterion to evaluate the detection probability of a fluorophore in a thick imaged volume, we have shown that annular binary phase masks optimized using Fisher information are adequate for both the detection probability and the localization accuracy. Indeed, under the assumption of a low photon balance, the optimization criteria defined in Eqs. (15) and (20) lead to similar optimal masks. Conversely, if the photon balance is large, the use of a mask optimized for detection is not necessary and the one optimized for localization only slightly degrades the detection probability. This result supports the common design practice consisting of optimizing a phase mask with a criterion based solely on localization accuracy. In other words, annular binary phase masks for DoF extension in single-molecule localization microscopy can be optimized using only a criterion based on Fisher information.

Although the formalism used in this paper assumes that the masks have circular symmetry (since they depend only on the radial coordinate r), the methodology developed can be easily extended to masks without particular symmetry. An interesting perspective of this work will therefore be to apply this methodology to other mask architectures, in order to verify the generalization of the conclusions that we have reached for masks with annular binary phase.

Disclosures. The authors declare no conflicts of interest.

References

1. M. Lelek, M. T. Gyparaki, G. Beliu, F. Schueder, J. Griffié, S. Manley, R. Jungmann, M. Sauer, M. Lakadamyali, and C. Zimmer, "Single-molecule localization microscopy," Nat. Rev. Methods Primers **1**, 39 (2021).
2. P. Jouchet, C. Cabriel, N. Bourg, M. Bardou, C. Poüs, E. Fort, and S. Lévêque-Fort, "Nanometric axial localization of single fluorescent molecules with modulated excitation," Nat. Photonics **15**, 297–304 (2021).
3. M. Xiu, J. Field, R. Bartels, and A. Pezeshki, "Fisher information and the Cramér-Rao lower bound in single-pixel localization microscopy with spatiotemporally modulated illumination," J. Opt. Soc. Am. A **40**, 185–203 (2023).
4. B. Hajj, M. El Beheiry, I. Izeddin, X. Darzacq, and M. Dahan, "Accessing the third dimension in localization-based super-resolution microscopy," Phys. Chem. Chem. Phys. **16**, 16340–16348 (2014).
5. P. Bon, J. Linarès-Loyez, M. Feyeux, K. Alessandri, B. Lounis, P. Nassoy, and L. Cognet, "Self-interference 3D super-resolution microscopy for deep tissue investigations," Nat. Methods **15**, 449–454 (2018).
6. F. Xu, D. Ma, K. P. MacPherson, S. Liu, Y. Bu, Y. Wang, Y. Tang, C. Bi, T. Kwok, A. A. Chubykin, P. Yin, S. Calve, G. E. Landreth, and F. Huang, "Three-dimensional nanoscopy of whole cells and tissues with in situ point spread function retrieval," Nat. Methods **17**, 531–540 (2020).
7. S. R. P. Pavani and R. Piestun, "Three dimensional tracking of fluorescent microparticles using a photon-limited double-helix response system," Opt. Express **16**, 22048–22057 (2008).
8. Y. Shechtman, S. J. Sahl, A. S. Backer, and W. E. Moerner, "Optimal Point Spread Function Design for 3D Imaging," Phys. Rev. Lett. **113**, 133902 (2014).
9. A. G. Godin, J. A. Varela, Z. Gao, N. Danné, J. P. Dupuis, B. Lounis, L. Groc, and L. Cognet, "Single-nanotube tracking reveals the nanoscale organization of the extracellular space in the live brain," Nat. Nanotechnol. **12**, 238–243 (2017).
10. O. Lévêque, C. Kulcsár, A. Lee, H. Sauer, A. Aleksanyan, P. Bon, L. Cognet, and F. Goudail, "Co-designed annular binary phase masks for depth-of-field extension in single-molecule localization microscopy," Opt. Express **28**, 32426–32446 (2020).
11. Q. Gresil, A. Lee, O. Lévêque, K. Caicedo, B. M. Muñoz, C. Kulcsár, F. Goudail, P. Bon, and L. Cognet, "A Binary Annular Phase Mask to Regulate Spherical Aberration and Allow Super-Localization in Single-Particle Tracking over Extended Depth-of-Focus," (2023). Submitted to Optics Communications.
12. C. Paviolo, F. N. Soria, J. S. Ferreira, A. Lee, L. Groc, E. Bezard, and L. Cognet, "Nanoscale exploration of the extracellular space in the live brain by combining single carbon nanotube tracking and super-resolution imaging analysis," Methods **174**, 91–99 (2020). Progress in Super-resolution Fluorescence Microscopy.
13. A. Bhattacharyya, "On a measure of divergence between two statistical populations defined by their probability distributions," Bull. Calcutta Math. Soc. **35**, 99–109 (1943).
14. O. Lévêque, C. Kulcsár, A. Lee, P. Bon, L. Cognet, and F. Goudail, "On the validity domain of maximum likelihood estimators for depth-of-field extension in single-molecule localization microscopy," J. Opt. Soc. Am. A **39**, 37–43 (2022).
15. M. Born and E. Wolf, *Principles of Optics: Electromagnetic Theory of Propagation, Interference and Diffraction of Light* (Cambridge University Press, 1999), 7th ed.
16. J. W. Goodman, *Introduction to Fourier optics* (W.H. Freeman & Company, 2017), 4th ed.
17. E. R. Dowski and W. T. Cathey, "Extended depth of field through wave-front coding," Appl. Opt. **34**, 1859–1866 (1995).

18. F. Diaz, F. Goudail, B. Loiseaux, and J.-P. Huignard, "Comparison of depth-of-focus-enhancing pupil masks based on a signal-to-noise-ratio criterion after deconvolution," J. Opt. Soc. Am. A **27**, 2123–2131 (2010).
19. J. Neyman, E. S. Pearson, and K. Pearson, "IX. On the problem of the most efficient tests of statistical hypotheses," Philos. Transactions Royal Soc. London. Ser. A, Containing Pap. a Math. or Phys. Character **231**, 289–337 (1933).
20. T. M. Cover and J. A. Thomas, *Information Theory and Statistics* (John Wiley & Sons, Ltd, 2005), chap. 11, pp. 347–408.
21. H. Chernoff, "A Measure of Asymptotic Efficiency for Tests of a Hypothesis Based on the sum of Observations," The Annals Math. Stat. **23**, 493–507 (1952).
22. A. Jain, P. Moulin, M. Miller, and K. Ramchandran, "Information-theoretic bounds on target recognition performance based on degraded image data," IEEE Transactions on Pattern Analysis Mach. Intell. **24**, 1153–1166 (2002).
23. F. Goudail, P. Réfrégier, and G. Delyon, "Bhattacharyya distance as a contrast parameter for statistical processing of noisy optical images," J. Opt. Soc. Am. A **21**, 1231–1240 (2004).
24. J. Kennedy and R. Eberhart, "Particle swarm optimization," in *Proceedings of ICNN'95 – International Conference on Neural Networks,* vol. 4 (1995), pp. 1942–1948.
25. R. Falcón, F. Goudail, C. Kulcsár, and H. Sauer, "Performance limits of binary annular phase masks codesigned for depth-of-field extension," Opt. Eng. **56**, 1–12 (2017).
26. Y. Zhou and G. Carles, "Precise 3D particle localization over large axial ranges using secondary astigmatism," Opt. Lett. **45**, 2466–2469 (2020).